nature geoscience

LETTERS

PUBLISHED ONLINE: 7 MARCH 2016 | DOI: 10.1038/NGEO2669

Remote sensing evidence for an ancient carbon-bearing crust on Mercury

Patrick N. Peplowski[1]*, Rachel L. Klima[1], David J. Lawrence[1], Carolyn M. Ernst[1], Brett W. Denevi[1], Elizabeth A. Frank[2], John O. Goldsten[1], Scott L. Murchie[1], Larry R. Nittler[2] and Sean C. Solomon[2,3]

Mercury's global surface is markedly darker than predicted from its measured elemental composition. The darkening agent, which has not been previously identified, is most concentrated within Mercury's lowest-reflectance spectral unit, the low-reflectance material[1]. This low-reflectance material is generally found in large impact craters and their ejecta[2,3], which suggests a mid-to-lower crustal origin. Here we present neutron spectroscopy measurements of Mercury's surface from the MESSENGER spacecraft that reveal increases in thermal-neutron count rates that correlate spatially with deposits of low-reflectance material. The only element consistent with both the neutron measurements and visible to near-infrared spectra[4] of low-reflectance material is carbon, at an abundance that is 1–3 wt% greater than surrounding, higher-reflectance material. We infer that carbon is the primary darkening agent on Mercury and that the low-reflectance material samples carbon-bearing deposits within the planet's crust. Our findings are consistent with the formation of a graphite flotation crust from an early magma ocean[5], and we propose that the heavily disrupted remnants of this ancient layer persist beneath the present upper crust. Under this scenario, Mercury's globally low reflectance results from mixing of the ancient graphite-rich crust with overlying volcanic materials via impact processes or assimilation of carbon into rising magmas during secondary crustal formation.

Mercury's most common spectral unit, the intermediate plains, reflects ~27% less sunlight than the lunar highlands and ~14% less than the mare-basalt-dominated lunar nearside[1]. On the Moon, reflectance (observed radiance divided by solar irradiance) varies inversely with the concentrations of Fe-rich pyroxene and opaque minerals—principally ilmenite ($FeTiO_3$)—at the surface. Mercury's surface is depleted in these darkening agents (FeO <2–3 wt%; ref. 6, Fe <2.5 wt%, Ti <1 wt%; refs 7–9), and there is no evidence for a correlation between Fe concentration and reflectance[9]. Lunar reflectance also decreases with optical maturation (darkening and reddening) of the regolith by space weathering[10]. Immature materials on Mercury have half the reflectance of fresh lunar highland materials[11,12], requiring that Mercury's surface hosts a darkening agent that does not play an important role in darkening the Moon.

Mercury's darkening agent should be most concentrated within Mercury's lowest-reflectance spectral unit[1,2,4], the low-reflectance material (LRM). The reflectance of LRM is ~30% below the global mean, and visible to near-infrared spectra reveal a broad depression, centred at a wavelength of ~600 nm, that is distinctive to LRM (Fig. 1). These data, and the inferred locations of LRM source regions beneath the volcanic plains that make up Mercury's upper crust[2,3], provide the basis for three proposed darkening agents[4]: carbon in the form of fine-grained endogenic graphite, a mixture of microphase and nanophase Fe or FeS formed by impact shock of pre-existing materials, or a mixture of Fe- and C-rich material delivered before widespread volcanic resurfacing of the planet. Ilmenite is ruled out because there is insufficient Ti in LRM (ref. 4). Each of the proposed darkening agents corresponds to a distinct prediction for the elemental composition of LRM deposits relative to their surroundings—that is, an enrichment in C, no major differences in elemental composition, or elevated C and Fe concentrations.

The MErcury Surface, Space ENvironment, GEochemistry, and Ranging (MESSENGER) spacecraft payload included the Gamma-Ray and Neutron Spectrometer[13] (GRNS) and the X-Ray Spectrometer[14] (XRS). GRNS and XRS data have been used to characterize the elemental composition of Mercury's surface[7–9,15], but so far there have been no spatially resolved measurements of Fe or C for LRM. The Neutron Spectrometer (NS), a subsystem of the GRNS, is sensitive to relative variations in the abundances of Fe and C. In particular, fluxes of low-energy ($E_n < 1$ eV) 'thermal' neutrons are inversely proportional to the macroscopic neutron-absorption cross-section (Σ_a) of materials within ~1 m of the surface[16,17]. Σ_a is the abundance-weighted sum of the individual (microscopic) neutron-absorption cross-sections (σ_a) for each constituent of the surface. Fe has a σ_a value of 2.56 barns (b; $1\,\text{b} = 1 \times 10^{-24}\,\text{cm}^2$), markedly higher than σ_a values for most other major elements (for example, Si, Mg, Al, Ca; $\sigma_a \sim 0.06$ to 0.5 b; see Supplementary Table 2). In contrast, C has a σ_a value of 3.5×10^{-3} b. C-enriched LRM would therefore appear as a local thermal-neutron enhancement[18], whereas LRM enriched in Fe and C relative to Mercury's mean surface abundances would manifest as lower thermal-neutron fluxes provided that the Fe/C ratio is >0.3.

We have examined NS data acquired over three LRM deposits (A–C) shown in Fig. 1. These deposits are each ~100 km across and were spatially resolved by the NS during low-altitude (<100 km) observations made during MESSENGER's final year of operations. LRM A is associated with the rim and central peak of the 106-km-diameter crater Akutagawa (centred at 48.2° N, 219.1° E). LRM B is within the ejecta of the 195-km-diameter crater Sholem Aleichem (50.9° N, 269.7° E). LRM C is a larger (~200 × 100 km) region centred at approximately 50° N, 300° E and located within the expected locations of ejecta from the Borealis and Derzhavin–Sor Juana basins[19]. We defined large ($>10^6\,\text{km}^2$) study areas (SAs; Supplementary Figs 1–3) centred on each LRM

---

[1]The Johns Hopkins University Applied Physics Laboratory, Laurel, Maryland 20723, USA. [2]Department of Terrestrial Magnetism, Carnegie Institution of Washington, Washington, DC 20015, USA. [3]Lamont-Doherty Earth Observatory, Columbia University, Palisades, New York 10964, USA.
*e-mail: Patrick.Peplowski@jhuapl.edu

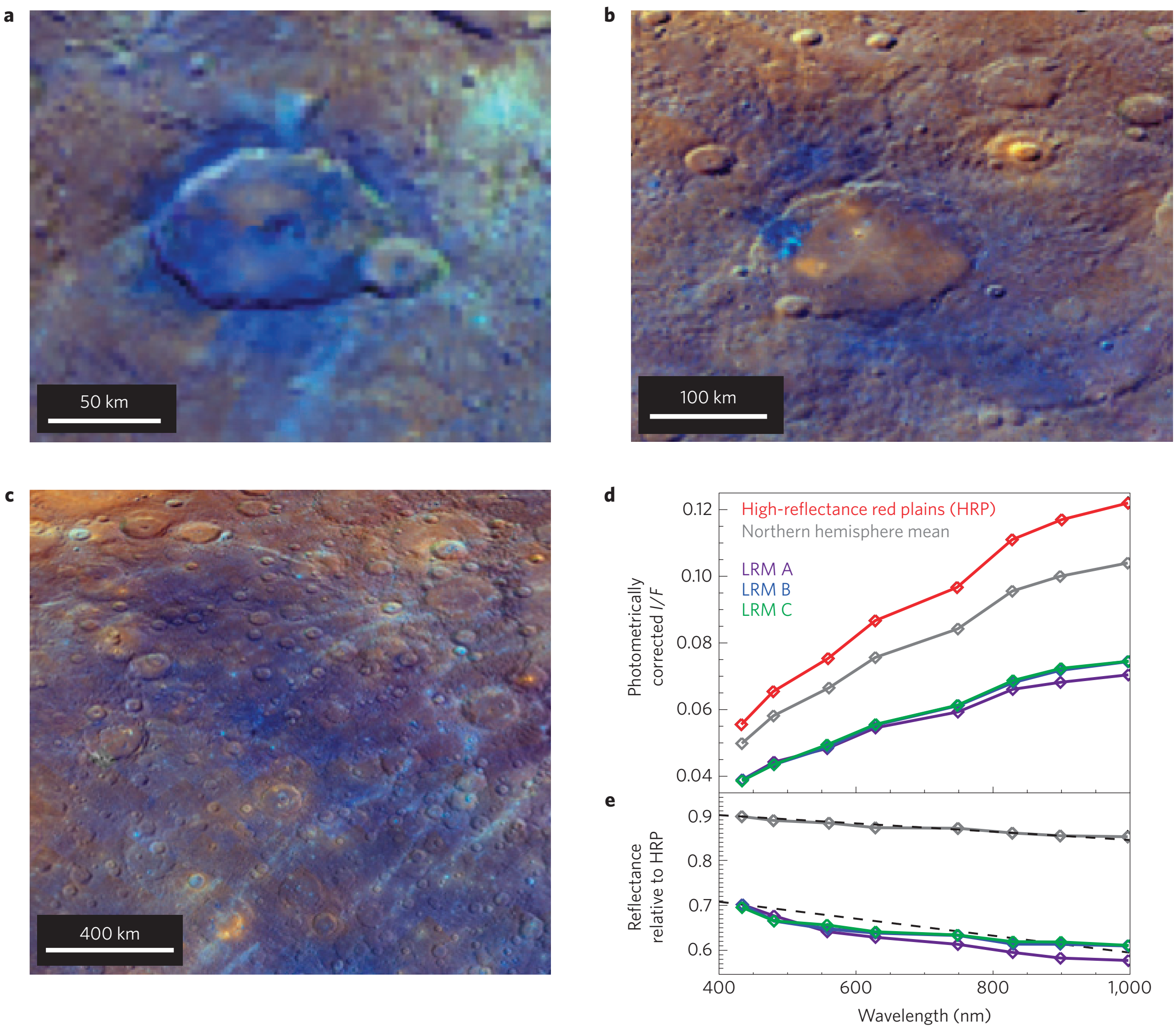

Figure 1 | Visible to near-infrared spectral properties of LRM. a–c, Enhanced-colour images of the LRM A, B and C deposits, respectively, which appear dark blue. The colour combination is based on a principal component (PC) analysis of a MESSENGER global eight-colour map (Methods) and places PC2, PC1 and the ratio of the reflectance at 430 nm wavelength to that of 1,000 nm in the red, green and blue channels, respectively. The images are simple cylindrical projections. **d**, Reflectance spectra (observed radiance, *I*, divided by solar irradiance, *F*) for the LRM deposits, the mean northern hemisphere and high-reflectance red plains (HRP; ref. 4). **e**, LRM and mean northern hemisphere spectra relative to HRP. Dashed lines connect the ratios at 433 and 900 nm and emphasize the absorption-like feature at ~600 nm.

deposit, and we queried the NS data set to identify orbits with low-altitude measurements of these areas. LRM deposits comprise a small areal fraction of the SAs, which include surrounding materials of higher reflectance for comparison. We processed the NS data that met viewing geometry criteria with a ~300-km-baseline low-pass filter (LPF) on an orbit-by-orbit basis to remove systematic variability (see Methods). We subtracted the output of the LPF from the measured count rates as a form of high-pass filter (HPF) to seek residual variations in neutron count rates at spatial scales <300 km. Examples of processed measurements are shown in Fig. 2.

Although each orbit contains hundreds of NS measurements, few (<4 per orbit) sample LRM, and no single measurement is statistically robust at the three-standard-deviation (3-σ) level. Fortunately, MESSENGER acquired repeated measurements over the three SAs treated here, including 308, 1,006 and 602 distinct 20-s measurements for SAs A, B and C, respectively. Of these, 6, 36 and 97 measurements sampled the LRM A, B and C deposits. Histograms of the SA-sampling HPF data are shown in Fig. 3. For each SA, the complete data set clusters around a residual value of zero, indicating that there is no systematic variability in the concentrations of neutron-flux-modifying absorbers at spatial scales <300 km. The measurements that sample only LRM, however, cluster about positive residual values, indicating a local increase in thermal-neutron production and a corresponding decrease in Σ_{a}.

The XRS instrument acquired one spatially resolved Fe measurement of an LRM deposit, LRM C, during a moderate-size solar flare. These data reveal a low Fe concentration (Fe/Si ~ 0.04) compared with an adjacent, non-LRM measurement (Fe/Si ~ 0.07; see Supplementary Fig. 3). Other measurements of LRM deposits have been acquired during non-flare conditions, when elemental detections were limited to Mg, Al and Si. Those results suggest an association between LRM and increased Mg/Si (for example, at LRM A and the Rachmaninoff LRM deposit[15]), although this trend is not detected at LRM B and C (see Supplementary Figs 1–3).

The neutron measurements indicate that LRM is compositionally distinct, but these data alone cannot be used to identify the darkening agent. All the LRM observations together—that is, elevated thermal-neutron count rates, lower Fe/Si concentrations within LRM C, consistently low reflectance, and the presence of the 600-nm absorption feature[4]—were required to identify graphitic carbon as the darkening agent. We compared the neutron

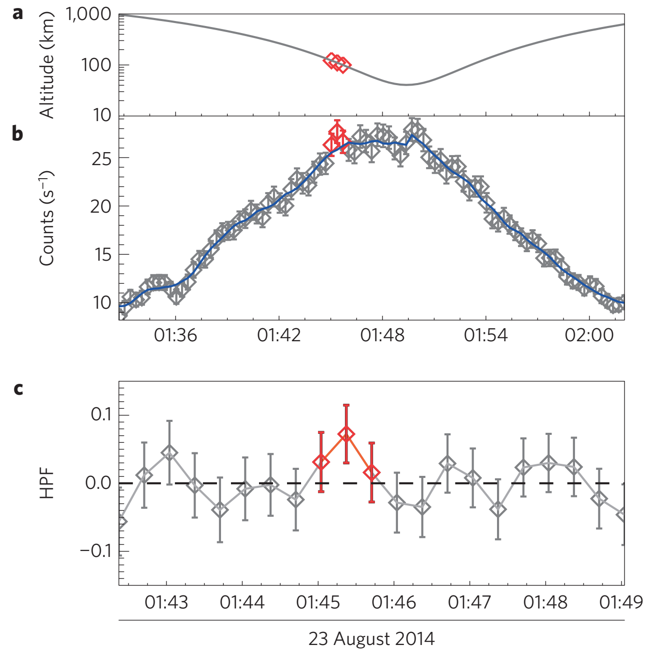

Figure 2 | NS time-series measurements acquired at altitudes <1,000 km over study area C. Orbit 3372 sampled study area (SA) C, and those data sampling LRM C are highlighted in red. **a**, Altitude of the spacecraft, which tracks the dominant source of systematic variability. **b**, Raw NS-measured neutron count rates for the thermal-sensitive detector (<1,000 km altitude), with the output of the low-pass filter (LPF) shown in blue. Error bars indicate one-standard-deviation statistical uncertainties. **c**, The residual neutron count rate after applying a high-pass filter (HPF) to measurements over SA C, including a two-standard-deviation residual detection within the LRM.

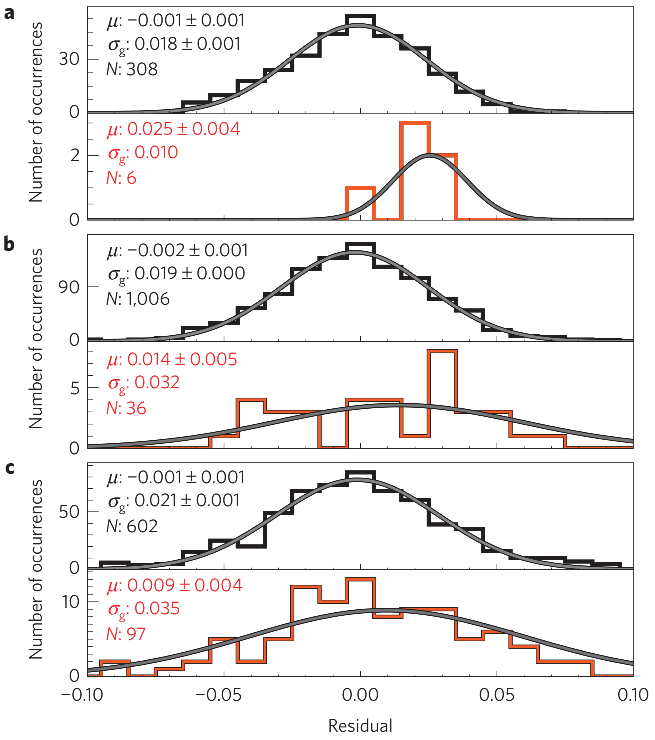

Figure 3 | Histograms of residual neutron measurements for each study area. All data for each SA are shown in black; data that sampled an LRM deposit are shown in red. **a**–**c**, Data from study areas A, B and C, respectively. For each histogram, a Gaussian function with a mean value μ and a width σ_g is used to characterize the population of size N (grey line; see Methods). In all three cases the LRM-sampled data show a positive mean residual (μ), corresponding to localized increases in thermal-neutron count rates and a distinctive elemental composition (Table 1).

residuals with modelled count rates[16–18,20] for materials that have varying C concentrations to estimate the enhancement in C within LRM (δC) that is required to reproduce our measurements (see Supplementary Fig. 6). The results, which span a one-standard-deviation range of 1.1–3.1 wt% C, are listed in Table 1 for each LRM deposit. We find that the δC concentrations track with the depth of the 600-nm absorption feature, but not overall reflectance (Table 1), which is also influenced by optical maturity.

Mercury's global spectral properties require that a darkening agent must be present in all surface materials, not just LRM. Our neutron measurements characterize relative variability; therefore, the reported C concentrations are relative to the mean values in each SA. The absolute C abundance within LRM is thus expected to be higher than the values given in Table 1. Modelling[4] of the single-scattering albedo of linear mixtures of C and Mercury's high-reflectance endmember—high-reflectance red plains[1,2] (HRP)—indicates that Mercury's mean northern hemisphere can be represented as HRP plus $\sim$1 wt% C, consistent with GRNS estimates[18]. LRM spectra were modelled as HRP plus $\sim$5 wt% C, which is slightly higher than our inferred concentrations of 2.1–4.1 wt% C (LRM δC ranges, Table 1, plus a nominal 1 wt% C in non-LRM). The sensitivity of the spectral modelling to the unknown grain size of the darkening phase may explain the discrepancy. We note that weight percent concentrations of C on Mercury contrast sharply with the concentrations observed on Earth, the Moon, Mars and Vesta (0.001–0.1 wt%; ref. 21).

The stratigraphic setting of the LRM is an important clue for determining the origin of Mercury's C. Following the methodology of a previous study[3], we estimate that the source region for LRM A is at least 4 km thick and has a burial depth of <6.3 km. For LRM B, we estimate a burial depth of <11.8 km. These observations are comparable with the depth extent of LRM source regions beneath the Rudaki plains and the Titian and Caloris basins[3,22]. The proximity of LRM A to Sobkou Planitia, and of LRM B and LRM C to several large basins, means that the LRM deposits considered here may have experienced multiple episodes of exposure and burial. Global modelling of impact-induced mixing suggests that the LRM darkening agent was ultimately derived from a chemically distinct lower crust that was $\sim$30 km beneath Mercury's surface[23], but given the disruptive effects of the late heavy bombardment (LHB) and a presumably long history of intrusive magmatism, source regions of LRM are likely to have been laterally discontinuous and compositionally heterogeneous.

A gradual infall of C-rich (15–25 wt%) cometary dust has been suggested as a source of Mercury's darkening component[24]. This idea would have to be modified from the original proposal, however, to account for the association of enhanced levels of C with impact-excavated material (that is, LRM). In particular, delivery of C-bearing material would need to have been higher before most volcanic resurfacing of the planet to account for the stratigraphy of the LRM (ref. 10). MESSENGER data indicate Fe/C ratios of $\sim$1 globally, and of <1 within LRM. In contrast, typical (non-cometary) solar system materials[21] have Fe/C ratios $\gg$ 1, so high-C content objects such as comets would need to have dominated the earliest material delivered to Mercury to account for an interior LRM source region by this scenario.

The stratigraphic setting of the LRM most readily supports an endogenous origin for Mercury's carbon. Given Mercury's present surface chemistry, graphite is the only buoyant mineral in any

Table 1 | Thermal-neutron signals and spectral properties for the LRM study areas.

	Neutron measurements			Spectral properties	
Study area[*]	**LRM residual[†]**	**Significance**	**δCarbon content[‡]**	**I/F (%) at 560, 750 nm[§]**	**600-nm band depth[‖]**
A	+2.6 ± 0.4%	$6.3\,\sigma$	$+2.8^{+0.3}_{-0.3}$ wt%	4.8 ± 0.3, 5.9 ± 0.4	2.2 ± 0.9%
B	+1.6 ± 0.5%	$3.1\,\sigma$	$+2.3^{+0.4}_{-0.5}$ wt%	4.9 ± 0.2, 6.1 ± 0.3	1.4 ± 0.9%
C	+1.0 ± 0.4%	$2.4\,\sigma$	$+1.6^{+0.5}_{-0.5}$ wt%	4.9 ± 0.2, 6.1 ± 0.2	1.0 ± 0.8%

[*] See Supplementary Figs 1–3 for details on the study areas. [†] Residual neutron count rate in LRM-sampling measurements, relative to all measurements in the study area. [‡] One-standard-deviation range of inferred C concentrations in LRM, relative to the mean composition in the study area (see Supplementary Fig. 6). [§] Observed radiance (I) divided by solar irradiance (F), derived from photometrically corrected Mercury Dual Imaging System (MDIS) data. [‖] Band depth relative to HRP. Derived from the mean MDIS BD630b parameter (central wavelength average at 550, 630, 750 and 830 nm wavelength with the continuum tied at 480 and 900 nm; ref. 10) within LRM deposits as defined in Supplementary Fig. 7.

early global magma ocean[5]. As such, graphite would accumulate as a flotation crust analogous to the Moon's primary feldspathic crust[5]. This crust is estimated to have been up to ~1 km thick, depending on the assumed C content of Mercury's bulk silicate fraction[5]. Mercury's present crust is the result of impact gardening of primordial crust, extensive volcanic resurfacing[9], magmatic intrusions, and impact melting and gardening of younger volcanic and plutonic materials. These processes, including impact mixing and assimilation of sub-surface material by rising magmas, would dilute any primordial crust through vertical and horizontal mixing with surrounding materials, providing plausible mechanisms for producing a surface with an average C concentration of ~1 wt%. In this scenario, the exposed LRM has a composition that is more similar to Mercury's primordial crust than that of the younger volcanic plains units. It may ultimately be possible to account for LRM—along with Mercury's unusually large core, high volatile element abundances[25], and chemically reduced composition[7]—with a C-rich accretional environment[26].

Methods

Methods and any associated references are available in the online version of the paper.

Received 18 August 2015; accepted 4 February 2016;
published online 7 March 2016

References

1. Robinson, M. S. *et al*. Reflectance and color variations on Mercury: regolith processes and compositional heterogeneity. *Science* **321,** 66–69 (2008).
2. Denevi, B. W. *et al*. The evolution of Mercury's crust: a global perspective from MESSENGER. *Science* **324,** 613–618 (2009).
3. Ernst, C. M. *et al*. Exposure of spectrally distinct material by impact craters on Mercury: implications for global stratigraphy. *Icarus* **209,** 210–223 (2010).
4. Murchie, S. L. *et al*. Orbital multispectral mapping of Mercury with the MESSENGER Mercury Dual Imaging System: evidence for the origin of plains units and low-reflectance material. *Icarus* **254,** 287–305 (2015).
5. Vander Kaaden, K. E. & McCubbin, F. M. Exotic crust formation on Mercury: consequences of a shallow, FeO-poor mantle. *J. Geophys. Res.* **120,** 195–209 (2015).
6. Blewett, D. T. *et al*. A comparison of the mercurian reflectance and spectral quantities with those of the Moon. *Icarus* **129,** 217–231 (1997).
7. Nittler, L. R. *et al*. The major-element composition of Mercury's surface from MESSENGER X-ray spectrometry. *Science* **333,** 1847–1850 (2011).
8. Evans, L. G. *et al*. Major-element abundances on the surface of Mercury: results from the MESSENGER Gamma-Ray Spectrometer. *J. Geophys. Res.* **117,** E00L07 (2012).
9. Weider, S. Z. *et al*. Variations in the abundance of iron on Mercury's surface from MESSENGER X-Ray Spectrometer observations. *Icarus* **235,** 170–186 (2014).
10. Hapke, B. Space weathering from Mercury to the asteroid belt. *J. Geophys. Res.* **106,** 10039–10073 (2001).
11. Denevi, B. W. & Robinson, M. S. Mercury's albedo from Mariner 10: implications for the presence of ferrous iron. *Icarus* **197,** 239–246 (2008).
12. Braden, S. E. & Robinson, M. E. Relative rates of optical maturation of regolith on Mercury and the Moon. *J. Geophys. Res.* **118,** 1903–1914 (2013).
13. Goldsten, J. O. *et al*. The MESSENGER Gamma-Ray and Neutron Spectrometer. *Space Sci. Rev.* **131,** 339–391 (2007).
14. Schlemm II, C. E. *et al*. The X-Ray Spectrometer on the MESSENGER spacecraft. *Space Sci. Rev.* **131,** 393–415 (2007).
15. Weider, S. Z. *et al*. Evidence for geochemical terranes on Mercury: global mapping of major elements with MESSENGER's X-Ray Spectrometer. *Earth Planet. Sci. Lett.* **416,** 109–120 (2015).
16. Lawrence, D. J. *et al*. Identification and measurement of neutron-absorbing elements on Mercury's surface. *Icarus* **209,** 195–209 (2010).
17. Peplowski, P. N. *et al*. Geochemical terranes of Mercury's northern hemisphere as revealed by MESSENGER neutron measurements. *Icarus* **253,** 346–363 (2015).
18. Peplowski, P. N. *et al*. Constraints on the abundance of carbon in near-surface materials on Mercury: results from the MESSENGER Gamma-Ray Spectrometer. *Planet. Space Sci.* **108,** 98–107 (2015).
19. Fassett, C. I. *et al*. Large impact basins on Mercury: global distribution, characteristics, and modification history from MESSENGER orbital data. *J. Geophys. Res.* **117,** E00L08 (2012).
20. Lawrence, D. J. *et al*. Evidence for water ice near Mercury's north pole from MESSENGER neutron spectrometer measurements. *Science* **339,** 292–296 (2013).
21. Lodders, K. & Fegley, B. Jr *The Planetary Scientist's Companion* (Oxford Univ. Press, 1998).
22. Ernst, C. M. *et al*. Stratigraphy of the Caloris basin, Mercury: implications for volcanic history and basin impact melt. *Icarus* **250,** 413–429 (2015).
23. Rivera-Valentin, E. G. & Barr, A. C. Impact-induced compositional variations on Mercury. *Earth Planet. Sci. Lett.* **391,** 234–242 (2014).
24. Bruck Syal, M., Schultz, P. H. & Riner, M. A. Darkening of Mercury's surface by cometary carbon. *Nature Geosci.* **8,** 352–356 (2015).
25. Peplowski, P. N. *et al*. Radioactive elements on Mercury's surface from MESSENGER: implications for the planet's formation and evolution. *Science* **333,** 1850–1852 (2011).
26. Ebel, D. S. & Alexander, C. M. O'D. Equilibrium condensation from chondritic porous IDP enriched vapor: implications for Mercury and enstatite chondrite origins. *Planet. Space Sci.* **59,** 1888–1894 (2011).

Acknowledgements

We thank the entire MESSENGER team for their invaluable contributions to the development and operation of the spacecraft. The MESSENGER mission is supported by the NASA Discovery Program under contracts NAS5-97271 to The Johns Hopkins University Applied Physics Laboratory and NASW-00002 to the Carnegie Institution of Washington. D.J.L. acknowledges support from the MESSENGER Participating Scientist Program.

Author contributions

P.N.P. led the data reduction and interpretation, as well as the development of this manuscript. R.L.K. led the spectral analysis of LRM. D.J.L. produced the data sets used in this analysis and developed the modelling codes. C.M.E. led the analysis and interpretation of LRM stratigraphy. J.O.G. led the design and assembly of the GRNS. L.R.N. and E.A.F. provided XRS data and interpretation. All authors assisted with the interpretation of the data and manuscript development, particularly B.W.D., S.L.M. and S.C.S.

Additional information

Supplementary information is available in the online version of the paper. Reprints and permissions information is available online at www.nature.com/reprints. Correspondence and requests for materials should be addressed to P.N.P.

Competing financial interests

The authors declare no competing financial interests.

Methods

Data set. Data sets used in this work are publicly available from the NASA Planetary Data System (PDS) at http://pds.nasa.gov. MESSENGER NS Calibrated Data Records (CDRs; ref. 27) are available at http://pds-geosciences.wustl.edu/missions/messenger/grns.htm. CDRs are pre-filtered[28] to remove measurements compromised by solar particle events and energetic electron events, which lower the signal-to-background ratio of neutron measurements. NS CDRs are time series aggregates of individual neutron measurements (spectra) and include peripheral ephemeris and detector information (for example, sensor temperature, power), catalogued by day of acquisition. We supplemented CDRs with the time derivatives of the spacecraft altitude, orientation vectors and velocity vectors as needed to filter the final data set (see Data filtering). NS measurements acquired with data accumulation times of 4 s (typical at altitudes <1,000 km during the final year of operations) were summed to create measurements with a total collection time of 20 s, the nominal NS data collection interval for the MESSENGER mission.

CDRs used in this study were acquired during MESSENGER's second extended mission (XM2; 18 March 2013–17 March 2015) as well as XM2′, the final extended mission (18 March 2015–30 April 2015). XM2 and XM2′ were the only periods during which MESSENGER achieved the orbital altitudes (<100 km) necessary to resolve the LRM deposits treated here with the NS. Data are limited to those acquired during orbits on which the spacecraft overflew one of three study areas (SAs), labelled A–C and shown in Supplementary Figs 1–3. Each SA included a ~100-km-scale deposit of LRM. Geologic and geochemical context for each SA, presented in Supplementary Figs 1–3, was created from PDS products.

LRM was identified from multispectral imaging measurements acquired with MESSENGER's Mercury Dual Imaging System[29] (MDIS). LRM is defined as regions with a photometrically corrected reflectance of <5% (at 560 nm wavelength) and a second principal component (PC2) of 0.006–0.023 calculated from a global eight-colour map. PC2 captures the diversity of slopes and curvature of spectral reflectance versus visible to near-infrared wavelength exhibited across Mercury, and the selected values highlight regions that are significantly lower ('bluer') in slope than the average for Mercury, a diagnostic signature of LRM (refs 2,4). LRM spectra are shown in Fig. 1, and a map of LRM is shown in Supplementary Fig. 4.

On a spectrum-by-spectrum basis, we flagged NS measurements to indicate data acquired when an LRM deposit was within the NS field of view. Flags were derived from a smoothed version of the LRM map. The smoothing[30] approximates the effective distribution as observed by NS, for which the spatial resolution is a factor of ~1.5 greater than the spacecraft altitude. The mean altitudes over each SA resulted in a smoothing radius of 35, 40 and 45 km for SA A, B and C, respectively. LRM flags were populated when the sub-spacecraft point contained >15% or more LRM (by area) from the smoothed map. The mean and standard deviation of the fraction of the NS footprint area filled with LRM for SA A, B and C are 20 ± 4%, 29 ± 13% and 46 ± 35%.

The spectral attributes of the LRM deposits examined in this study were derived from MDIS visible to near-infrared spectra (Fig. 2). Spectra were photometrically corrected to a standard viewing geometry of 30° incidence angle, 0° emergence angle and 30° phase angle[29]. Table 1 lists the band depth of the 600-nm absorption-like feature as well as the reflectance for each deposit. Band depth is derived from the MDIS BD630b parameter[4], which is calculated as the central wavelength average in the 550-, 630-, 750- and 830-nm filter channels relative to a continuum tied to the 480-nm and 900-nm channels. Reflectance values are reported as the quotient of the measured radiance (I) and the solar flux (F) multiplied by 2π.

Regions of the surface included in each LRM spectrum are shown in Supplementary Fig. 4. Note that a small (northernmost) portion of LRM C was omitted from the spectral analysis but not the neutron analysis. MDIS spectra (Fig. 1) reveal that LRM A has the lowest I/F and largest band depth of the three deposits examined here, suggesting that the darkening agent may be more concentrated in LRM A than LRM B and C, which have higher I/F values and shallower band depths (Table 1). These observations are consistent with the neutron data, as LRM A has the strongest neutron enhancement, and by inference the highest C concentration, despite the fact that this deposit was less represented (by area) in the NS footprints than LRM B and C.

Data systematics. NS measurements are dominated by systematic variability that obscures signatures of compositional variations on the surface (Fig. 2 and Supplementary Figs 5 and 6). Sources of systematic variation include altitude dependence of the neutron signal, sensor orientation relative to Mercury, and the orientation of the NS relative to the spacecraft velocity vector. To quantify these effects, we adopt the standard spacecraft coordinate frame[31], in which the x-axis is parallel to the rotation axis of the spacecraft solar arrays, the y-axis is along the Magnetometer boom, and the $-z$-axis is in the direction of the large velocity adjust thruster. The $+z$ deck of the spacecraft is generally planet-facing for altitudes <~2,000 km.

The NS is composed of two lithium glass (LG) sensors (10 × 10 × 0.4 cm) located on opposite sides of a (10 cm; ref. 3) cube of borated plastic scintillator[12]. Thermal neutrons are detected with the LG plates, for which the normal is parallel to the spacecraft x-axis. Owing to Doppler enhancements resulting from the comparable speeds of the spacecraft and thermal neutrons[32], the LG sensors are most sensitive to thermal neutrons when their normal is aligned with the spacecraft velocity vector. This condition is quantified by the projection of the spacecraft velocity ($\mathbf{V}$) onto the spacecraft's unit x-axis vector ($\mathbf{e}_x$), calculated as $\mathbf{V} \cdot \mathbf{e}_x$ and hereafter denoted as V_x.

Example NS measurements (Fig. 2 and Supplementary Figs 5 and 6) highlight the dependence of the thermal-neutron signal on the spacecraft-to-planet distance (altitude), detector orientation relative to the planet (represented by the nadir angle θ_n between the spacecraft-to-planet vector and the z-axis of the spacecraft), and V_x. The dependence of the neutron count rates on altitude, apparent in Fig. 2 and Supplementary Fig. 5, is straightforward: the neutron flux (events per unit area) decreases with increasing distance from Mercury. The dependence on orientation is also apparent in Supplementary Fig. 5, where an abrupt (and temporary) change of orientation (θ_n from ~0° to ~40°) resulted in a temporally correlated increase in measured count rates. Note that positive θ_n values correspond to mostly unobstructed views for the NS and congruently higher count rates, whereas for negative θ_n values the spacecraft body is between the NS and Mercury, resulting in attenuation of neutrons and a reduction in measured count rates.

The dependence of the NS signals on V_x is highlighted in Supplementary Fig. 6. When V_x is positive, LG1 is facing the direction of 'oncoming' thermal neutrons, and it therefore is thermal-neutron enhanced. When V_x is negative, LG2 is the thermal-neutron-enhanced detector. For the majority of the orbit depicted in Supplementary Fig. 6, V_x was less than approximately −0.6, and LG2 had higher count rates than LG1. An abrupt (and temporary) change in V_x to approximately −0.2 was correlated with a change in relative count rates, as LG1 became the higher-count-rate detector.

Note that there is also a time dependence to the NS measurements, as the neutron-inducing galactic cosmic ray (GCR) flux is variable. Our decision to treat the data on an orbit-by-orbit basis (see section 'Low-pass filtering') eliminates the need to consider inter-orbit variability in the GCR flux. Sub-orbit (<8 h timescale) changes to the GCR flux can, in principle, affect our measurements, but the fact that we used data acquired over one year of operations makes that scenario unlikely. GCRs would have to have systematically increased during LRM-sampling measurements (and/or decreased during non-LRM-sampling measurements) to produce our result.

Finally, there is a vertical Doppler enhancement to thermal-neutron measurements[16,20]. This phenomenon creates an asymmetry in the inbound and outbound portions of the orbit, although our reported measurements were acquired before and around periapsis, limiting the impact of this asymmetry. This effect is handled by our low-pass filter.

Data filtering. For each study area, we queried the NS CDRs to identify orbits during which the NS acquired measurements within that study area and that have altitudes <200 km, $\theta_n > -15°$, and $|V_x| > 0.2$. The altitude criterion removes orbits for which NS data have insufficient spatial resolution to resolve LRM deposits. The nadir angle requirement ($\theta_n > -15°$) restricts spacecraft obscuration effects (see Supplementary Section 2.1 and Supplementary Fig. 5). The V_x criterion ensures that one of the two LG detectors has enhanced thermal-neutron count rates. On an orbit-by-orbit basis, the count rates from the detector with the thermal-neutron enhancement were used in our analysis. Any orbit containing at least three individual measurements meeting these criteria was passed (in full) to the next stage of the analysis.

Low-pass filtering. On an orbit-by-orbit basis, we applied an LPF consisting of a six-measurement-wide moving boxcar average of the data (see Fig. 2b). The six-measurement (120 s) baseline corresponds to a ground track distance of ~300 km. The LPF captures the low-frequency systematics of the NS measurements (for example, most variations with attitude) as well as large-scale (>300-km) compositional variability. Variations on horizontal scales <300 km are characterized with the HPF (see Fig. 2).

Rapid changes in spacecraft ephemeris (relative to the 120 s smoothing baseline) can produce HPF signals that mimic variable surface composition. We characterized this possibility with a model data set (see NS count-rate model), which confirmed the validity of our LPF/HPF analysis technique (Supplementary Table 1) provided that the occasional measurements acquired during rapid changes in spacecraft ephemeris are removed from consideration.

Histograms of the HPF data for each SA, including separate treatment for those measurements that sampled LRM, are shown in Fig. 3. Data in the histograms are limited to those acquired at altitudes <100 km (required to spatially resolve LRM A-, B- and C-sized features), and for $\theta_n > -12°$, a more effective cutoff suggested on the basis of the modelled count rates. For all measurements within each study area, we fit the data to a Gaussian distribution, $y = Ae^{[-(x-\mu)^2/2\sigma_g^2]}$, where x and y are HPF (residual) and number of values, respectively, and A is area, μ the population mean, and σ_g the distribution width. The LRM-only data generally do not include sufficient measurements to reliably fit for all three parameters (A, μ, σ_g), so we instead empirically calculated μ and σ_g following standard procedures[33]. We then fit the function to determine A using the calculated μ and σ_g values. For all cases, the uncertainty in the population mean μ, σ_μ, was calculated as the standard error of the mean, $\sigma_\mu = \sigma_g/\sqrt{N}$, where N is the number of samples in each population (see Fig. 3; ref. 33).

The results of these fits are shown in Fig. 3. Comparison of measured and modelled histograms indicate that the non-LRM measurements follow the expected behaviour for a population for which variability is dominated by counting statistics (see Supplementary Table 1). The difference between the LRM and non-LRM population means ($\delta\mu$, denoted 'LRM residual' in Table 1) was determined as the difference between the μ values for each population as $\mu(\mathrm{LRM}) - \mu(\mathrm{All})$. The uncertainty for $\delta\mu$, $\sigma_{\delta\mu}$, was calculated by adding the errors for both μ values (σ_μ) in quadrature. The statistical significance of the residual (significance, Table 1) was calculated as $\delta\mu/\sigma_{\delta\mu}$.

NS count-rate model. We used an existing toolkit[16,17,20], based on the radiation transport code Monte Carlo N-Particle eXtended (MCNPX; ref. 34), to simulate GCR-induced neutron production in Mercury's surface material[35] and neutron transport to[32,36] and detection by[16] the NS. These models reproduce the systematic variability observed in the NS measurements[16,20] and provide a means of relating measured neutron count rates to surface composition. Our models are calculated as a time series identical to the NS CDRs. The models provided two inputs to this analysis: validation of the LPF methodology and conversion of LRM residuals to estimates of carbon concentrations (Table 1).

The modelled count rates were calculated for a uniform surface composition, and as a result the application of our data reduction process (LPF, HPF) to the model should yield a null result—that is, no positive mean residuals for the LRM-sampling 'measurements'. The model therefore provides a mechanism to test the data reduction process and identify (and remove) any systematics that it introduces into the analysis. We subjected our modelled measurements to the same filtering as the NS data set, and then we ran the filtered model set through the LPF analysis. Examination of the HPF residuals for the model showed null residuals for the vast majority of measurements. Exceptions were identified for (modelled) count rates sampled during periods of rapid changes in spacecraft attitude that should be omitted from the LPF. Specifically, we found that measurements made when $|\mathrm{d}V_x/\mathrm{d}t| > 0.012\,\mathrm{km\,s^{-2}}$ or $|\mathrm{d}\theta_\mathrm{n}/\mathrm{d}t| > 1.65^\circ\,\mathrm{s^{-1}}$ should be omitted from the LPF to produce a zero-residual HPF for the model. The need for these criteria is straightforward: when the spacecraft rapidly (relative to the 120-s baseline of the LPF) changed orientation in a way that affected the neutron measurements, high-frequency changes in the neutron count rates result and manifest as residuals in the HPF data. In addition, the models suggest that $\theta_\mathrm{n} < -12^\circ$ is a better cutoff than our original data criterion ($\theta_\mathrm{n} < -15^\circ$), motivating the removal of those measurements before constructing histograms of the residuals.

Residuals for the modelled count rates for each study area are listed in Supplementary Table 1, both as raw output from the model (Simulations—No Statistics column) and modified to include Poisson statistical uncertainties (Simulations—Poisson Statistics column). There are no significant residuals for the LRM in our modelled data set, justifying our data selection criteria and confirming that our analysis methodology does not introduce systematic variability that could be mistaken for a chemical signature at the surface.

Derivation of carbon concentrations. Our measurements (LRM residuals, Table 1) show that thermal-neutron count rates are elevated over each of the LRM deposits examined in this study. Thermal-neutron count rates are (inversely) proportional to surface composition via the macroscopic neutron-absorption cross-section (Σ_a). Σ_a is a bulk chemical parameter, calculated as the weighted sum of all element-specific microscopic neutron-absorption cross-sections (σ_a) for the chemical constituents of Mercury surface materials as

$$\Sigma_a = N_\mathrm{A} \sum_i \frac{w_i}{A_i}\sigma_i \qquad (1)$$

in units of cm^2 g^{-1}, where N_A is Avogadro's number (6.022×10^{23} atoms mol^{-1}), A_i is the atomic mass of element i, σ_i is the σ_a value for each element i taken from previous modelling of Mercury's neutron production[12], and w_i is the weight fraction of element i.

σ_a values, listed in Supplementary Table 2, quantify the probability that an element will absorb a neutron. Our measured residuals (Fig. 3, Table 1) are evidence for thermal-neutron enhancements that are spatially correlated with LRM deposits, but the data are not element specific. The addition of the XRS- and MDIS-derived constraints indicates that the element in question is carbon (in the form of graphite to satisfy MDIS observations). Carbon's low σ_a value (3.5×10^{-3} b) compared with more abundant elements such as Si, Mg, Al and Ca (0.165, 0.063, 0.235, 0.436 b, respectively) explains why a C-enriched material will have enhanced thermal-neutron emission.

Deriving a carbon concentration (relative to non-LRM regions) from the measured residuals for each LRM deposit requires input from the neutron model, as neutron generation, moderation, and transport to and detection by the NS are sufficiently complex to prohibit characterizing elemental composition directly from the neutron measurements. We created a series of models based on a mean composition for Mercury surface material, but with C concentrations of 0, 1, 3 and 5 wt%. The models were calculated for the SA 3 data set and were subsequently subjected to the LPF analysis in a manner identical to that applied to the NS data. The residuals for each model are plotted as a function of C content (relative to the 0 wt% C case) in Supplementary Fig. 7. A third-order polynomial was fitted to the results, and that polynomial was used to convert measured residuals to C concentrations. Although this relationship was derived only from the LRM C data set, the viewing geometries were similar for all study areas, so this model set was used to derive C concentrations from NS residuals for all three regions.

Measurements of a high-reflectance region. If carbon is Mercury's global darkening agent (Supplementary Fig. 8), then high-reflectance regions should have depleted C content, which will manifest as a local low in thermal neutrons. To test this hypothesis, we repeated our analysis for one of Mercury's highest-reflectance regions, the Rachmaninoff pyroclastic deposit[37] (PD). I/F values for the PD (~9.5 at 950 nm, ~11.5 at 750 nm) are significantly higher than for the LRM deposits (Table 1). We repeated our data analysis procedures for the PD, modified to allow for measurements taken at altitudes up to 200 km because of a lack of lower-altitude flyovers of the region. We identified seven NS measurements with footprints that substantially overlapped the PD. A histogram of the data, shown in Supplementary Fig. 9, includes 1,350 measurements in the PD study area (34° N–39° N latitude; 62° E–68° E longitude) and the seven PD-sampling measurements. The data reveal a relative decrease in thermal-neutron count rates ($-1.4 \pm 0.8\%$) over the PD, consistent with reduced C concentrations ($\delta\mathrm{C} \sim -1.0$–$2.0$ wt%) and supporting the hypothesis that C is Mercury's global darkening phase.

Code availability. MCNPX was developed by the Los Alamos National Laboratory. It is available to US citizens from https://mcnpx.lanl.gov. Analyses were performed using IDL (Interactive Data Language; www.exelisvis.com/IDL). Data fitting was done with the IDL MPFIT package (available from https://www.physics.wisc.edu/~craigm/idl/fitting.html).

References

27. Lawrence, D. J. & Ward, J. G. *MESSENGER Neutron Spectrometer Calibrated and Derived Data Record Software Interface Specification* (NASA Planetary Data System Geosciences Node, 2013); http://pds-geosciences.wustl.edu/messenger/mess-e_v_h-grns-3-ns-cdr-v1/messns_2001/document/ns_cdr_ddr_sis.pdf
28. Lawrence, D. J. *et al*. Comprehensive survey of energetic electron events in Mercury's magnetosphere with data from the MESSENGER Gamma-Ray and Neutron Spectrometer. *J. Geophys. Res.* **120,** 2851–2876 (2015).
29. Klima, R. L. *et al*. Global distribution and spectral properties of low-reflectance material on Mercury. In *47th Lunar Planet. Sci. Conference* Abstract 1195 (Lunar and Planetary Institute, 2016); http://www.hou.usra.edu/meetings/lpsc2016/pdf/1195.pdf.
30. Peplowski, P. N. *et al*. Enhanced sodium abundance in Mercury's north polar region revealed by the MESSENGER Gamma-Ray Spectrometer. *Icarus* **228,** 86–95 (2014).
31. McAdams, J. V. *et al*. MESSENGER mission design and navigation. *Space Sci. Rev.* **131,** 219–246 (2007).
32. Feldman, W. C. & Drake, D. M. A Doppler filter technique to measure the hydrogen content of planetary surfaces. *Nucl. Instrum. Methods A* **245,** 182–190 (1986).
33. Bevington, P. R. & Robinson, D. K. *Data Reduction and Error Analysis for the Physical Sciences* 2nd edn edn (WCB/McGraw-Hill, 1992).
34. Pelowitz, D. B. (ed.) *MCNPX User's Manual v. 2.5.0.* Report LA-UR-94-1817 (Los Alamos National Laboratory, 2005).
35. McKinney, G. W. *et al*. MCNPX benchmark for cosmic ray interactions with the Moon. *J. Geophys. Res.* **111,** E06004 (2006).
36. Feldman, W. C. *et al*. Gravitational effects on planetary neutron flux spectra. *J. Geophys. Res.* **94,** 513–525 (1989).
37. Prockter, L. M. *et al*. Evidence for young volcanism on Mercury from the third MESSENGER flyby. *Science* **329,** 668–671 (2010).